Demonstration of hot-spot fuel gain exceeding unity in cryogenic direct-drive inertial confinement fusion implosions

C. A. Williams,[1,2,a)] R. Betti,[1,2,3] V. Gopalaswamy,[1] J. P. Knauer,[1] C. J. Forrest,[1] A. Lees,[1] R. Ejaz,[1,3] P. S. Farmakis,[1,3] D. Cao,[1] P. B. Radha,[1] K. S. Anderson,[1] S. P. Regan,[1,3] V. Yu Glebov,[1] R. C. Shah,[1] C. Stoeckl,[1] S. Ivancic,[1] K. Churnetski,[1,3] R. T. Janezic,[1] C. Fella,[1] M. J. Rosenberg,[1] M. J. Bonino,[1] D. R. Harding,[1] W. T. Shmayda,[1] J. Carroll-Nellenback,[1,2] S. X. Hu,[1] R. Epstein,[1] T. J. B. Collins,[1] C. A. Thomas,[1] I. V. Igumenshchev,[1] V. N. Goncharov,[1,3] W. Theobald,[1,3] K. M. Woo,[1] J. A. Marozas,[1] K. A. Bauer,[1] S. Sampat,[1] L. J. Waxer,[1] D. Turnbull,[1] P. V. Heuer,[1] H. McClow,[1] L. Ceurvorst,[1] W. Scullin,[1] D. H. Edgell,[1] M. Koch,[1] D. Bredesen,[1] M. Gatu Johnson,[4] J. A. Frenje,[4] R. D. Petrasso,[4] C. Shuldberg,[5] M. Farrell,[5] J. Murray,[5] D. Guzman,[5] B. Serrato,[5] S. F. B. Morse,[1] M. Labuzeta,[1] C. Deeney,[1] and E. M. Campbell[1]

[1)]*Laboratory for Laser Energetics, University of Rochester, Brighton, New York 14623*

[2)]*Department of Physics and Astronomy, University of Rochester, Rochester, New York 14627*

[3)]*Department of Mechanical Engineering, University of Rochester, Rochester, New York 14627*

[4)]*Plasma Science and Fusion Center, Massachusetts Institute of Technology, Cambridge, Massachusetts 02139*

[5)]*General Atomics, San Diego, CA 92121*

By irradiating small capsules containing deuterium and tritium fuel with intense laser light, an implosion is generated that creates a plasma hot enough to initiate fusion reactions. We report on the first set of experiments in laser direct drive to release more fusion energy than the amount of energy in the central hot-spot plasma, or a hot-spot fuel gain $G_{\rm hs}$ above unity. While this was accomplished first in indirect drive using up to 1.9 MJ of laser energy[1] (to generate $G_{\rm hs} \sim 4$), the present achievement was realized with laser energy as low as 28 kJ on the Omega Laser System. The hot-spot fuel gain is predicted to grow with laser energy and target size. Therefore, the results presented in this work establish the direct-drive approach to inertial fusion as a promising path toward burning and ignited plasmas in the laboratory. Additionally, we present the results of the first thin-ice DT liner targets to be imploded on OMEGA, which led to a fusion energy yield of 0.9 kJ, a new record for the Omega Laser System.

In laser-driven inertial confinement fusion[2–4] (ICF), energy is rapidly coupled to the surface of a capsule containing cryogenic deuterium–tritium (DT) fuel, which causes its outermost layer to ablate and the remaining spherical shell to implode via momentum conservation (i.e., the "rocket effect"). This energy deposition could come in the form of near-ultraviolet laser light (direct drive)[5], or the soft x rays of a blackbody radiation field, generated when a high-Z hohlraum is heated by a laser (indirect drive)[6]. In general, direct-drive ICF can be viewed as a series of energy transfer steps; laser energy is absorbed via inverse bremsstrahlung in the target's tenuous plasma corona, then carried to the dense fuel payload by electron thermal conduction, and subsequently converted into kinetic energy of the imploding shell. The final transfer process occurs when the kinetic energy of the shell becomes internal energy of the central "hot-spot" plasma, and the dense DT shell is halted by the hot spot's rising pressure. As the shell reaches stagnation, the hot spot acquires the requisite temperatures and densities to produce copious thermonuclear fusion reactions $\mathrm{D} + \mathrm{T} \rightarrow \mathrm{n}(14.03\,\mathrm{MeV}) + \alpha(3.53\,\mathrm{MeV})$.

In general, performance is improved either by designing a more-robust implosion, so that the adverse effects of hydrodynamic instabilities (namely Rayleigh–Taylor[7] and Richtmyer–Meshkov[8]) are lessened, or by enhancing the energy coupled to the capsule. The former method was the primary source of improvement for the Omega Laser Facility at the University of Rochester's Laboratory for Laser Energetics from 2016 to 2018, a period that saw the maximum neutron yield $Y_{\rm n}$ rise from 5×10^{13} to 1.5×10^{14}. This surge[9] was made possible through the use of statistical models[10,11], which allow individual, independent degradation mechanisms to be identified and addressed. The statistical models view the experimental yield as being given by the one-dimensional yield (using the radiation-hydrodynamic code *LILAC*[12]), multiplied by a series of degradation factors. These factors are determined by physically motivated design parameters, each used to pull out dependencies of associated modes of failure[13]. These include both small-scale perturbations (like capsule defects and instability seeds formed by the speckle pattern of individual beams), and large-scale perturbations such as beam mispointing and beam-to-beam power imbalance[5]. This statistical modeling approach is also currently being extended using a database of 2D (azimuthally symmetric) simulations using the Eulerian radiation-hydrodynamic code *DRACO*[14]. The utility of deep-learning neural networks is being explored as well[15].

While statistical modeling has been an indispensable tool for limiting yield degradation, yield is not the sole concern of experiments on the Omega Laser. The purpose of controlled fusion—whether confined magnetically or by mass inertia—is to generate the thermonuclear instability known as "ignition." In ICF, the onset of ignition occurs when fusion α particles deposit enough energy in the hot spot to outweigh losses due to thermal conduction, radiation, and when the hot spot eventually succeeds in repelling the Fermi-degenerate confining shell, the plasma expansion. Ignition leads to a rapid increase in the temperature of the hot spot, thereby driving a burn wave through the cold dense fuel that confines it[16,17]. A metric used

[a)]Electronic mail: cwilli86@ur.rochester.edu

to assess the proximity of an implosion to ignition is the Lawson criterion χ (with $\chi \approx 1$ corresponding to ignition), derived originally as $\chi \equiv (P\tau)/(P\tau)_{\text{ignition}}$, where P is hot-spot pressure and τ the confinement time[18]. The Lawson criterion can be recast[19] in terms of neutron yield (in units of 10^{16} neutrons), stagnated fuel mass (in mg), and areal density (in g/cm^2)

$$\chi = (\rho R)^{0.61} \left(\frac{0.12 Y_{16}}{M_{\text{stag}}} \right)^{0.34}, \tag{1}$$

and it is this form of χ that is used to gauge progress in OMEGA implosions. The laser energy available on OMEGA is insufficient to drive a fuel assembly with enough mass and areal density to ignite; OMEGA delivers ~30 kJ of UV light to tens of micrograms of fuel, while megajoules of driver energy and a fuel mass of the order of miligrams are required for hot-spot ignition (the target mass scales linearly with laser energy). For sub-ignition-scale experiments, theory and computation can be used to infer the yield that could be achieved with a more-energetic driver if the same core conditions produced on OMEGA were realized on the larger system, referred to as hydrodynamic scaling[20–22]. Note that hydrodynamic scaling takes into account only the geometric benefits of driving a larger system; if α particle deposition is considered, any increase in α heating comes as the result of the hot-spot volume growing proportional to the laser energy, not because of an increase in compression. When scaling up to the energy available on the National Ignition Facility (NIF), this essentially amounts to multiplying the OMEGA χ by a factor $(E_{\text{NIF}}/E_{\Omega})^{1/3} \approx 4.2$.

The utility of the Lawson parameter, however, extends beyond that of a hydro scaling tool—it plays a crucial role in navigating the design space of modern OMEGA experiments from an energetics perspective. The fusion energy is given by

$$E_{\text{f}} = \varepsilon_{\text{f}} \int \text{d}t \int \text{d}^3 r \, n_{\text{D}} n_{\text{T}} \langle \sigma v \rangle, \tag{2}$$

where $\varepsilon_{\text{f}} = 17.6\,\text{MeV}$ is the energy released in one DT reaction, n_{D} and n_{T} are the deuteron and triton number densities, respectively, and $\langle \sigma v \rangle$ is the DT reactivity. It is assumed that the plasma is at a sufficiently high temperature and low enough density so as to be neither strongly coupled nor degenerate[4], which permits an ideal gas treatment for the hot-spot equation of state. Under this assumption, $E_{\text{f}} \sim \varepsilon_{\text{f}} (P^2/T^2) \langle \sigma v \rangle V_{\text{hs}} \tau$, where P and T are the plasma pressure and temperature, respectively, V_{hs} the hot-spot volume, and τ the burnwidth (duration). Manipulating this relation leads to

$$E_{\text{f}} \propto E_{\text{hs}} \left(\frac{P\tau}{T^2/\varepsilon_{\text{f}} \langle \sigma v \rangle} \right), \tag{3}$$

where E_{hs} is the internal energy of the hot spot. Recalling that $\chi \equiv (P\tau)/(P\tau)_{\text{ignition}}$ allows for a more transparent representation of the fusion yield to be arranged

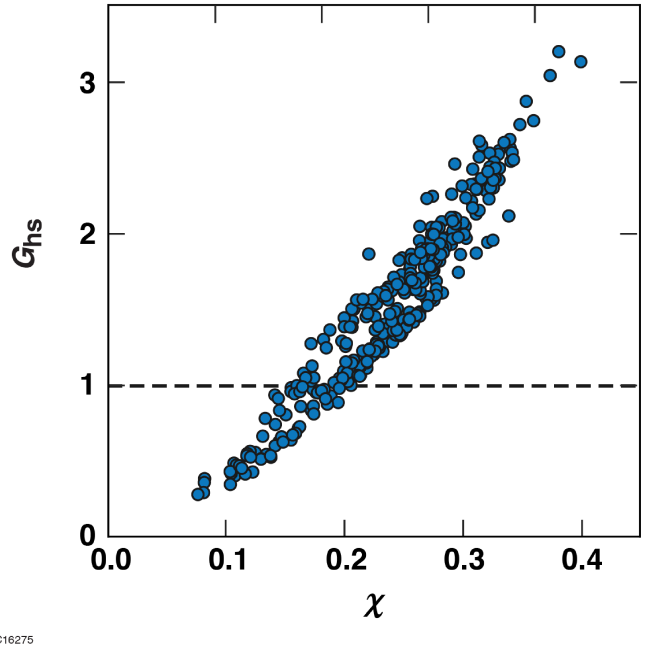

FIG. 1: Hot-spot gain versus Lawson parameter for a collection of *LILAC* simulations that span a wide range of design parameters (e.g., adiabat and IFAR). The $G_{\text{hs}} = 1$ threshold does not correspond to a unique value of χ, but occurs at $\chi = 0.18$ for both linear and quadratic fits. On OMEGA, α heating has a negligible effect on yield and hot-spot energy, so χ may be calculated with α energy deposition turned off.

$$E_{\text{f}} \propto E_{\text{hs}} \chi. \tag{4}$$

Two main takeaways are readily apparent from equation (4). First, although the main function of the Lawson parameter is to gauge how close an implosion is to igniting, it also serves as a proxy for the *hot-spot fuel gain*, which we define as the ratio of fusion energy output to hot-spot internal energy $G_{\text{hs}} \equiv E_{\text{f}}/E_{\text{hs}}$. The constant of proportionality between G_{hs} and χ can be determined from simulations. Figure 1 displays an ensemble of implosions simulated in *LILAC* with $\chi \leq 0.4$. Each data point corresponds to a post-shot simulation of an OMEGA experiment where the target specifications (size and layer thicknesses) and experimental laser pulse are fed directly into *LILAC*. For implosions on OMEGA, the hot spot is nearly transparent to the 3.5-MeV α particles born in DT fusion reactions, and escape the hot spot without slowing down and depositing their energy. Because the ion temperature, and hence, the yield, is minimally affected by α-heating, it has been turned off in the simulations presented in figure 1. A linear fit applied to these simulated data reveals

$$G_{\text{hs}} = 8.83\chi - 0.58,$$

which predicts hot-spot gain to equal unity when $\chi \approx 0.18$. In these simulations, shots begin surpassing $G_{\text{hs}} = 1$ when χ is as low as 0.15, while every shot satisfies the condition if

$\chi > 0.2$. The aforementioned improvements made by the statistical modeling approach not only tripled the yield, but also pushed χ to the region where $G_{\rm hs}$ on OMEGA would be expected to exceed 1.

The second important consequence of equation (4) is that further increases in yield (above the mark set in 2018) by factors of 2 or more on OMEGA necessitate a boost in $E_{\rm hs}$, specifically. This is because raising χ by similar factors could only realistically be achieved with a change in the experimental scale itself, which is to say, an entirely new driver with a drastic increase in energy.

The NIF has probed this area of parameter space for nearly a decade. The first experimental demonstration of fusion energy exceeding the energy coupled to the fuel was in indirect-drive experiments fielded on the NIF, reported on in 2014[1]. The implosions discussed in that work used $\sim$1.9 MJ of laser energy to transfer 3.5 to 4.4 kJ to the hot spot, ultimately resulting in 14.4 to 17.3 kJ of fusion energy. These experiments were also noteworthy because they released more fusion energy than the kinetic energy of the in-flight shell. It was also determined that shot N131119 from that study had a yield twice as high as what would have been generated in the absence of α heating, a key milestone on the path to creating laboratory burning plasmas[23], and eventually, ignition[24,25].

The current work details the first experiments to achieve hot-spot gain exceeding unity in cryogenic *direct-drive* ICF, accomplished on the OMEGA laser with pulse energy as low as 28 kJ, and negligible yield amplification from α heating. Achieving this result with a kilojoule-class laser has important implications for the prospect of pursuing ICF with megajoule-class lasers in a direct-drive format. In the companion paper to this current publication, Gopalaswamy *et al.*[26] assert that these most recent shots would produce 1.6$\pm$0.3 MJ if they were hydrodynamically scaled to use 2.15 MJ of direct-drive laser energy (the capacity of the NIF in indirect drive). In this work, we first address how the hot-spot energy is determined before discussing the adjustments that made the $G_{\rm hs} > 1$ feat possible, then summarize the impact of these results. Additionally, we explain the theoretical underpinnings of how the neutron yield was doubled in the latest OMEGA experiments, going from $\sim 1.6 \times 10^{14}$ at the beginning of 2021 to 3.1×10^{14} by the end of that year (which translates to the fusion energy increasing from 0.45 kJ to 0.88 kJ), a new record mark in cryogenic direct drive as well as the most fusion energy produced with a sub-megajoule-class laser.

Naturally, asserting with confidence that the fusion energy has surpassed the internal energy of the hot spot requires both of these values to be calculated in a reliable manner. In the case of the fusion energy, the calculation is relatively straightforward. Each DT fusion reaction produces a single 14-MeV neutron; determining the fusion energy is therefore tantamount to measuring the neutron yield[27]. A description of how the neutron yield is measured is given in Methods.

Discerning the hot-spot internal energy is less routine. To begin with, there is no one-to-one correlation between the hot-spot energy and a lone observable like there is in the case of fusion energy and neutron yield. Instead, we are left to infer the hot-spot internal energy by finding the spatial profile of the hot-spot pressure, and then integrate it throughout the hot-spot volume. Furthermore, the value that is ultimately settled on is influenced by the choice of theoretical model used for constraint. This work is not the first to infer the energy content of an ICF hot spot[28,29]. The model we have constructed, however, includes several features that are not typically included in such evaluations (a full description of the model used in this study is provided in the Methods section). The most meaningful additions are: (1) the inclusion of monotonically decreasing pressure profiles instead of isobaric (flat) profiles and (2) allowing the electron and ion temperatures to differ from one another. Momentum conservation leads to spatial variations in pressure when the implosion velocity is a significant fraction of the hot-spot sound speed, and electron and ion temperatures differ because their equilibration time is comparable to the burnwidth ($\sim$ 60 ps) in high-performance OMEGA implosions. Including both of these effects is essential if the hot-spot core conditions are to be obtained with the highest degree of accuracy. For the fastest implosions on OMEGA, the pressure at the edge of the hot spot can be as low as 50% of the value at the center[30], making evident the need for a non-isobaric model. Assuming thermal equilibration on OMEGA would artificially increase the hot-spot pressure by around 15%.

Instead of assuming an isobaric hot spot, or describing the radial profiles of the partial pressures and temperatures with analytic functions that are left unaltered across all shot designs, we have opted to take the *shape* of these profiles from *LILAC* simulations, and glean their magnitudes from observables acquired using neutron and x-ray diagnostics[27,31–34]. It is standard for models to eliminate the time dependence of temperature and pressure by introducing static profiles and replacing the temporal integral in equation (2) with the burnwidth. Our model does the same, but also institutes a correction factor on τ that handles deviations in the neutron production rate $\dot{Y}_{\rm n}(t)$ from that of a perfect Gaussian history.

Our model was first tested on synthetic experiments. We applied the model's procedure to the same database of simulated OMEGA experiments that was presented in figure 1 and used synthetic neutron and x-ray data from those same simulations to infer properties of the hot spot. The strong agreement between simulated hot-spot core conditions at bang time (the time of peak neutron production) and those inferred by the model is displayed in figure 2. Note that the model accurately recovers the state of the simulated hot spot across a remarkably diverse collection of shots. The outer diameters (OD's) in the set range from 760 μm to 1060 μm, while the ice thicknesses are as thin as 25 μm and as thick as 85 μm. The laser pulses used across the database are similarly varied. The dissimilar initial conditions lead to hot-spot environments that explore a wide parameter space; the central ion temperatures extend from 3 keV to 15 keV, while the pressures and energies span an order of magnitude across the database.

Many prior improvements in performance have revolved around stability and symmetry control, using techniques such as intentionally prescribing target offsets to mitigate low-mode asymmetries[35], or moving to smaller target outer diameters to promote better illumination uniformity. The adjust-

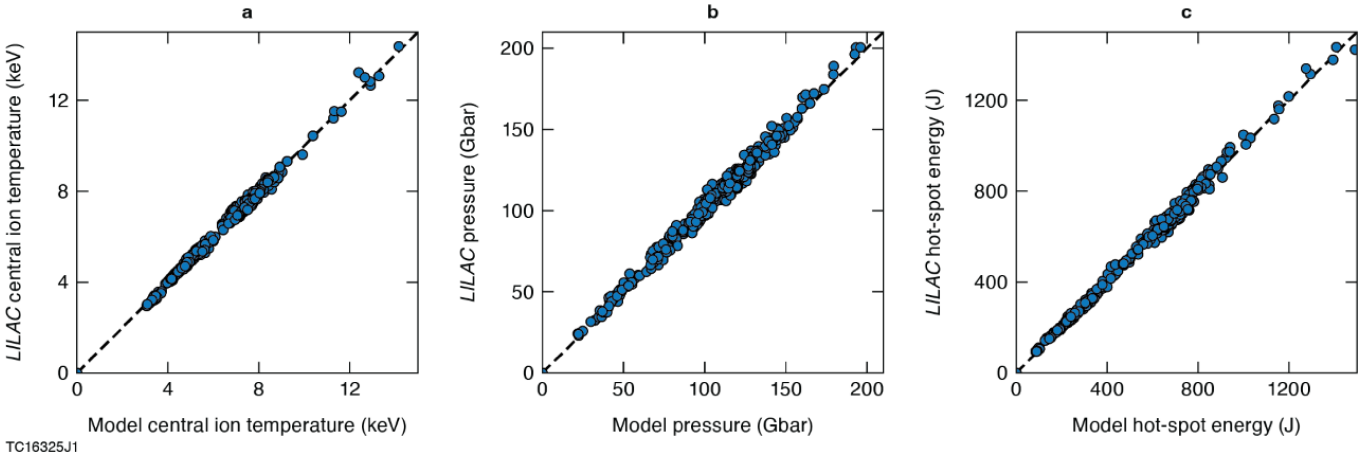

FIG. 2:
Bang time core conditions of OMEGA implosions simulated in *LILAC* compared to values gathered from the hot-spot inference model. Strong agreement is observed among a host of parameters, including a) central ion temperature, b) volume-averaged hot-spot pressure, and c) hot-spot internal energy over a wide range of values, revealing the model as being robust against changes in design parameters.

ments that followed, however, have focused primarily on one concept: coupling efficiency to the hot spot. We assert that by taking the model that constrains simulated data and applying it to experimental data, we should uncover the state of the hot spot and be able to track its response to design changes. To best understand the alterations that have facilitated the advancements described in this work, we will examine in greater detail the energy transfer chain from laser to hot spot described in the outset. Mathematically, this transfer process can be represented by the product of the laser energy E_{L} with three efficiencies η,

$$E_{\mathrm{hs}} = E_{\mathrm{L}}\eta_{\mathrm{abs}}\eta_{\mathrm{hydro}}\eta_{\mathrm{hs}}. \tag{5}$$

Here, η_{abs} is the absorption fraction, the hydrodynamic efficiency η_{hydro} is the conversion of absorbed energy to shell kinetic energy (rocket efficiency), and η_{hs} is the transfer of kinetic energy to internal energy of the hot spot. Short of major renovations to the laser itself, bumping the laser energy above the 28.5 kJ level that is consistently delivered on OMEGA requires greater conversion from the natural 1053 nm (infrared) line of an Nd:glass laser, to the frequency-tripled (3ω) ultraviolet light that irradiates the target. This is done by ramping up near the 30 TW limit earlier in the drive and compressing the pulses in time (shortening them below 2 ns), and/or employing the multipulse-driver technique, which turns off smoothing by spectral dispersion (SSD)[36] during the main drive. These improve frequency conversion efficiency, and can make available up to 31.5 kJ of UV energy, around 10 % higher than with full-bandwidth SSD on during the entire pulse. In addition to delivering more energy to the capsule surface, a dedicated effort to improve the effectiveness of the incident energy is equally important. The absorption fraction is diminished mainly by cross-beam energy transfer (CBET), which allows the light of incoming edge rays to be redirected into outgoing rays that are refracted away from the target[37]. One way to combat this is by imploding larger-OD capsules so more rays are normally incident on the target and less refract. However, this can have a negative effect on stability because it leads to higher in-flight aspect ratios (IFAR = shell radius/shell thickness) and lower beam-to-target radius ratios ($R_{\mathrm{b}}/R_{\mathrm{t}}$); both of these jeopardize the shell integrity and make it susceptible to ρR degradation and in-flight breakup[38]. Instead of increasing the outer diameter indefinitely, mid-Z dopants can be added to the ablator to foster greater collisional absorption of the incoming "pump" rays and higher coronal temperatures, which both reduce CBET[37]. Laser energy is transferred to the plasma by causing collisions between ions in the corona against electrons oscillating in the electric field of the laser light. The presence of a dopant like silicon (Z = 14), for example, facilitates a faster rate of collisions[4,39]. Adding as little silicon as 5 % to 7 % (by atomic fraction) has been shown to enhance absolute absorption on OMEGA by 10 % through "A/B" comparisons where the same laser pulse is used on targets with/without silicon. The inclusion of silicon serves the added benefit of diminishing the production of suprathermal electrons arising from the two-plasmon–decay instability[39,40], which prematurely heat the in-flight shell and cause it to decompress[41,42], leading to lower ρR and lower χ. Thus, silicon addresses various sources of degradation that limit G_{hs} while simultaneously raising the hot-spot and fusion energies above the implosions reported on by Gopalaswamy *et al.*[9] in 2019 that used similar pulses on glow-discharge polymer (GDP) ablators, referred to henceforth as "GDP χ-optimization".

Although generating more yield is an important factor in increasing χ, the designs that optimize χ do not necessarily optimize yield simultaneously. The latter consideration requires an approach that is more focused on 1D characteristics. In essence, this means optimizing the yield by augmenting coupling to the hot spot, even at the cost of slightly reducing χ. The thin-ice DT liner is a class of target devised by Williams *et al.*[30] explicitly for this purpose. These targets are intended to maximize energy absorption by putting as much as possible onto the largest-OD targets available. Figure 3 com-

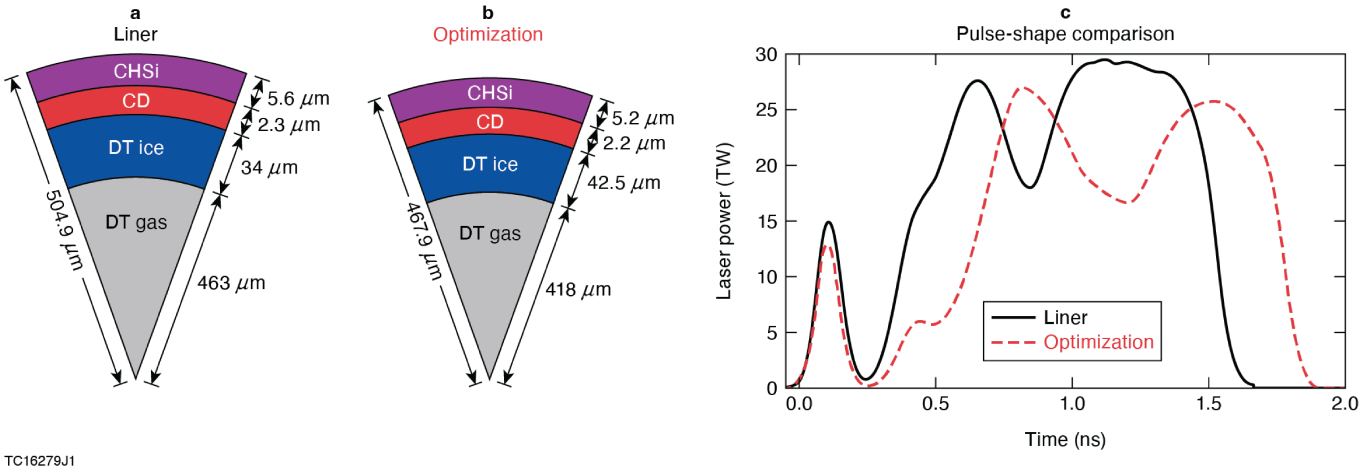

FIG. 3:

a) An example of a thin-ice DT liner target, whose outermost ablator layer is doped with silicon for better laser absorption and laser-plasma instability mitigation. The outer diameter of the liner is larger than the χ-optimization target in b), and its ice layer much thinner. This leads to an ultrahigh-velocity implosion ~600 km/s, in contrast to the ~500 km/s level accessed in χ-optimization shots. The 30.8 kJ MPD pulse of a DT liner is compared to the 28.5 kJ SSD pulse of a χ-optimization shot in c).

TABLE I: Experimental results of three high-performance OMEGA implosions. Determinations of hot-spot energy, central pressure and temperature, and χ are obtained using the 1D hot-spot inference model devised for this study. The initial ice thickness is denoted by Δ_{DT}, and the adiabat α is the ratio of plasma pressure to Fermi-degeneracy pressure during the acceleration phase. Brackets correspond to neutron averages. The ‡ symbol denotes a thin-ice DT liner.

Shot Number	OD/Δ_{DT} (μm)	E_f/E_{hs} (J)	χ	α	V_{hs} (10^5 μm^3)	[a] $\langle T_i\rangle/T_0$ (keV)	$\langle P\rangle/P_0$ (Gbar)
102154	935.3 / 44.5	627 / 603	0.19	5.1	0.61	4.7 / 6.6	73.6 / 76.3
‡102360[b]	1013.4 / 34.6	747 / 812	0.13	8.9	2.11	6.0 / 8.4	32.0 / 34.9
‡103952	1018.0 / 39.5	871 / 838	0.16	6.3	1.50	5.8 / 8.2	43.2 / 46.2

[a] Minimum measured ion temperature among a suite of neutron time-of-flight (nTOF) detectors located along various lines of sight.
[b] Only capsule without Si-dopant

pares a DT liner target with one meant to optimize the Lawson criterion (referred to as a χ-optimization target). Although silicon doping was not explored in the original liner design paper, the two concepts are fully compatible, which further enhances laser absorption. Additionally, because the payload velocity diverges logarithmically with remaining mass fraction (in the simple rocket model[4]), starting off with a thin ice layer boosts η_{hydro} and enables implosion velocities as high as 600 km/s. Because the mass ablation rate of indirect drive is roughly 10× higher than in direct drive (at 3ω), the hydrodynamic efficiency of laser-driven shells cannot compete with x-ray drive. Yet, direct-drive implosions make up for this gap by circumventing additional loss mechanisms that are present in indirect drive, such as finite hohlraum albedo (conversion of laser light to x-ray radiation). Additionally, an indirect-drive target sits in a radiation bath that is isotropic, and therefore never encounters many of the x rays present in the cavity. In totality, out of the 2 MJ initially incident on a NIF hohlraum, approximately 15 to 20 kJ ends up as fuel kinetic energy[43] (close to 30 kJ if the diamond ablator kinetic energy is added). The absorption in direct drive on OMEGA helps the shell acquire 1.5 to 2 kJ of kinetic energy, and is therefore ~5× more efficient at turning laser energy into kinetic energy.

One of the key components to realizing ignition on the NIF was improving the conversion of kinetic energy to internal energy by decreasing coast time in order to avoid early decompression of the shell[44]. This is because a thin, dense shell stagnates all at once like a hard piston, in contrast to a distended, puffy shell that struggles to do work on the hot spot[45]. The functional dependencies of the simulated transfer efficiency from shell-kinetic to hot-spot internal energy can be obtained from a nonlinear regression on the IFAR and the adiabat α. This is shown in figure 4a, where α is defined as the ratio of pressure in the shell to the Fermi-degenerate pressure of a fully ionized DT plasma at the shell density. The fit leads to the relation

$$\eta_{hs} = (0.0456)\mathrm{IFAR}^{0.85}\alpha^{0.22}. \quad (6)$$

A similar model can be formed using the implosion velocity ($\eta_{hs} \propto v_{imp}{}^{1.9}$), but the IFAR and adiabat are preferred since all three variables are dimensionless. These trends are corroborated in experiment, as illustrated by figure 4b, which shows that high-IFAR, ultrahigh-velocity liners are capable of

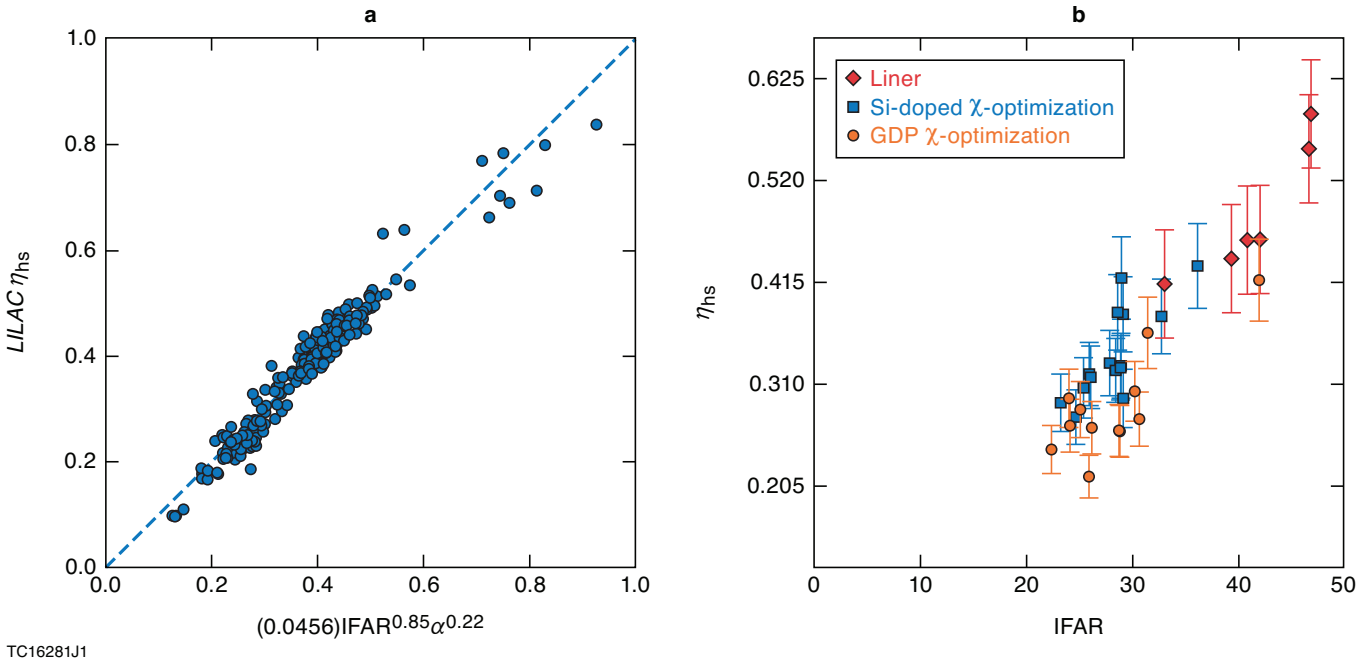

FIG. 4:

a) A predictive model for the transfer efficiency from shell kinetic energy to hot-spot internal energy η_{hs} in 1D simulations. The dotted line represents a perfect prediction. The only variables used to train this model are the in-flight aspect ratio (IFAR) and adiabat α, which finds $\eta_{hs} = (0.0456)\text{IFAR}^{0.85}\alpha^{0.22}$, although a similar model can be formed that finds $\eta_{hs} \propto v_{imp}{}^{1.9}$ b) Experimental values of the transfer efficiency from shell kinetic energy to hot-spot internal energy in OMEGA direct-drive implosions. The plot verifies that the in-flight aspect ratio (IFAR) is the dominant force in determining transfer efficiency. In experiment, unlike 1D simulations, low-mode perturbations also have an effect on transfer efficiency, as residual kinetic energy impedes efficient conversion to internal energy, and is responsible for the reduction in η_{hs}.

delivering the most energy to the hot spot. The transfer efficiency is reduced roughly 15% in experiment with respect to 1D simulations. Three-dimensional effects like low-mode asymmetries allow the shell to retain kinetic energy even at peak compression, which ultimately degrades hot-spot pressure and yield[46].

Table I gives a summary of experimental results from a selection of OMEGA implosions. Upon inspection, the table supports a number of expected trends. First, while the large IFAR values of liners gives rise to their elevated transfer efficiencies, the only way to stave off the instabilities that would otherwise break the shell apart is to raise their adiabat (entropy)[30,47–51]. This comes at the detriment of target convergence, which keeps their hot-spot pressure low. The liners are able to produce high yields in spite of these low pressures, not just because of the high temperature at the core, but because it remains above thermonuclear temperatures ($\sim$1 keV) out to a significant radius. In other words, what liners lack in terms of density, they make up for with sheer volume. For instance, the hot-spot volume of shot number 102360 is $\sim 3.5\times$ larger than shot number 102154, and produces more yield despite having less than half the hot-spot pressure. This realization gives added understanding to the high transfer efficiencies of liners displayed in figure 4; the extra energy coupled to the hot spot in liner implosions does not manifest as elevated energy density (pressure), but rather, it heats up a larger volume of plasma, in accordance with the predictions presented in Ref.[30]. Additionally, note that shot number 102360 falls below the χ range (0.15 to 0.2 according to figure 1) where G_{hs} is expected to surpass unity, which is validated experimentally. By contrast, shot numbers 102154 and 103952 have Lawson parameters that reside within this range, and indeed produce $G_{hs} > 1$.

In its current configuration, with beams that are less smooth than OMEGA and only directed along the poles of the target, the NIF is not a platform conducive for performing high-convergence direct-drive implosions. Therefore, the ability to realize large fusion energy outputs without requiring high convergence ratios to do so, makes thin-ice DT liners an attractive candidate for megajoule-class direct-drive implosions on the NIF. However, the low convergence does cause a reduction in χ, and is therefore detrimental to the hot-spot gain as well, but this effect can be combatted. By doping the ablator of liners like shot 103952 with silicon, more mass can be added to the fuel payload while maintaining implosion velocities of $\sim$600 km/s, which keeps the ion temperature high. The thicker ice layer decreases IFAR, allowing for the adiabat to be lowered concurrently without sacrificing stability. The lower adiabat recovers some of the pressure, as expected from 1D theory, and increases yield, χ, and hot-spot fuel gain. Thus, the OMEGA liner implosions serve as an example of how changes to the target and laser pulses can be used to in-

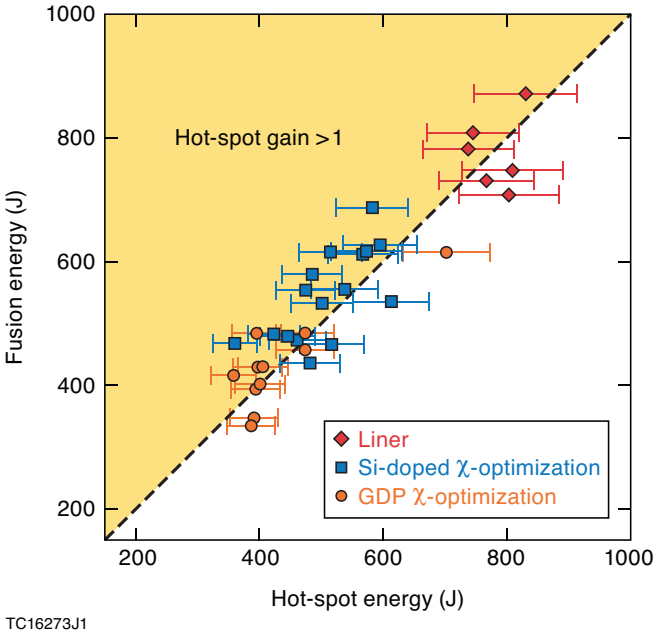

FIG. 5:

Fusion energy versus hot-spot energy in recent implosions on OMEGA. The figure shows hot-spot gain > 1 being achieved in campaigns intended to optimize χ with glow-discharge polymer (GDP) capsules, silicon-doped targets from the optimization campaign, and thin-ice DT liner targets intended to boost yield.

tentionally guide implosions toward specific goals, such as increasing temperature or decreasing hot spot volume.

When the hot-spot inference model is applied to the experimental database of past shots on OMEGA, it is revealed that a number of recent implosions, including thin-ice DT liners, demonstrate fusion outputs larger than the internal energy of the hot spot required to induce the fusion reactions therein. Recall that on OMEGA, heating of the hot spot comes almost exclusively from the piston-like compression performed by the surrounding dense shell; the dimensions of the hot spot are smaller than the mean-free-path of the 3.5-MeV α particles created in DT fusion reactions[4], and therefore the level of α heating generated in these implosions has a negligible effect on both the yield and internal energy. The importance of creating yield on the strength of compression alone is that it is a key ingredient even in ignition-scale implosions, because ignition is a dynamical process. If a hot spot is unable to produce a high reaction rate during the compression phase of the implosion, α deposition will be inconsequential even if the assembly is much larger than the α mean-free-path, since the energy carried by the fusion products will be negligible with respect to the hot-spot energy (which is why χ has an explicit yield dependence in equation (1) in addition to ρR). In every DT reaction, 20% of the energy release is imparted to the α particle, meaning $E_\alpha > 0.2E_{\rm hs}$ when $G_{\rm hs} > 1$.

As a consequence of equation (4), the slope of an $E_{\rm f}$ versus $E_{\rm hs}$ plot represents a measure of implosion quality, and is proportional to χ. Figure 5 shows the fusion energy plotted against the hot-spot energy for a series of recent OMEGA implosions, with a slight majority corresponding to $G_{\rm hs} > 1$. That this demonstration was realized with only ~30 kJ is significant because of the potential benefits that may lie in hydrodynamically scaled versions of these shots. While $E_{\rm hs}$ scales linearly with laser energy, the fusion energy scales faster, even in the absence of α heating. In 1D, $E_{\rm f} \propto E_{\rm L}{}^{1.43}$, primarily because the confinement time scales with target radius, but also because the temperature improves with size as a result of weaker thermal conduction losses; in spherical geometry, the ratio of surface area to volume grows with radius R like $1/R$, so the heat flux from hot spot to cold shell has a smaller impact on large targets. When α particle energy deposition becomes an important factor at ignition-relevant scales, it too has a more-pronounced effect on the fusion energy than it does on internal energy. This is because the energy of the hot spot is proportional to its temperature, while the temperature dependence of the reactivity is much stronger ($\langle\sigma v\rangle \propto T^4$ at a few keV)[4]. Even below the ignition threshold, it is possible for the main contribution to the hot-spot energy to come from α particle deposition, eclipsing the compression work done by the shell. This distinction, referred to as the burning plasma regime, is inaccessible on OMEGA due to the aforementioned energy deficit. However, Gopalaswamy *et al.*[26] report that the highest performing implosions on OMEGA have now entered a regime where, if hydroscaled to 2.15 MJ of laser drive, would produce a burning-plasma.

In conclusion, the results of the experiments discussed in this work demonstrate the ability to purposefully navigate throughout a parameter space created by laser, kinetic, internal, and fusion energy. An understanding of the way in which these forms of energy affect one another can benefit designs for future direct-drive facilities with energies potentially one or two orders of magnitude above the current capabilities of the Omega Laser Facility. Through enhanced laser coupling, implosions on OMEGA can now produce more fusion energy than the internal energy required to initiate the fusion reactions. This achievement is the first of its kind in a direct-drive format, and has been accomplished without the benefit of substantial yield amplification from α heating. This work also announces the first experimental results of thin-ice DT liner implosions, which were used to nearly double the previous facility record for neutron yield, taking it from 1.6×10^{14} at the beginning of 2021, to 3.1×10^{14} by year's end. Target alterations like silicon doping have also led to implosions with hot-spot pressures in the 80 Gbar range, a new high for the Omega Laser, and a marked improvement above the 50 Gbar milestone reported on in 2016 by Regan *et al.*[52] Future work to further increase the Lawson parameter of OMEGA implosions will focus on creating higher target convergence and generating pressures near 100 Gbar.

METHODS

Inferring Hot-Spot Energy

A direct measurement of the hot-spot internal energy in an ICF implosion is not feasible. However, this quantity can be

inferred if neutron and x-ray diagnostics are able to provide the necessary measurements to derive the hot-spot pressure from the neutron yield, ion temperature, and hot-spot volume. The latter is inferred from x-ray self-emission images.

The first measurable quantity of interest is the neutron yield Y_{n}. For thermonuclear plasmas, the specific reaction rate (reactions per unit volume, per unit time) R_{ij} between two species i and j is given by

$$R_{\mathrm{ij}} = \frac{n_{\mathrm{i}} n_{\mathrm{j}}}{1+\delta_{\mathrm{ij}}} \langle \sigma v \rangle_{\mathrm{ij}}, \tag{7}$$

where n_{i} is the number density of species i, $\langle \sigma v \rangle$ the reactivity of the reaction in question and δ_{ij} the Kroenecker delta. The total neutron yield from reactions between deuterium and tritium is obtained by integrating the specific reaction rate over time and space

$$Y_{\mathrm{n}} = \int \mathrm{d}t \int \mathrm{d}^3 r \, n_{\mathrm{D}} n_{\mathrm{T}} \langle \sigma v \rangle, \tag{8}$$

where the subscript has been dropped from the reactivity for brevity. Because the hot-spot plasma has a Coulomb coupling parameter $\Gamma \ll 1$, and is nondegenerate ($T_{\mathrm{i}} \gg T_{\mathrm{F}}$), we are able to use an ideal gas equation-of-state to relate the ion number density to the ion partial pressure and temperature $n_{\mathrm{i}} = P_{\mathrm{i}}/(k_{\mathrm{B}} T_{\mathrm{i}})$. We assume a single temperature for both ion species due to their relatively small mass difference, but allow for the composition of the plasma to differ from that of an equimolar mixture. The ion number density can then be substituted into the yield equation

$$Y_{\mathrm{n}} = \frac{f_{\mathrm{D}} f_{\mathrm{T}}}{{k_{\mathrm{B}}}^2} \int \mathrm{d}t \int \mathrm{d}^3 r \frac{{P_{\mathrm{i}}}^2}{{T_{\mathrm{i}}}^2} \langle \sigma v \rangle, \tag{9}$$

where f_{i} is the species fraction of species i and k_{B} is Boltzmann's constant.

Equation (9) can be simplified by substituting static profiles for time-dependent variables and replacing the integral over time with a finite burn duration factor. If the neutron production rate $\dot{Y}$ were a perfectly Gaussian function in time, replacing the temporal integral in equation (9) with the the burn-width τ (FWHM) would result in static profiles corresponding to a production rate $\dot{Y}_*$ that is larger than the bang-time rate $\dot{Y}_{\mathrm{bt}}$ by a factor $\sqrt{\pi/\ln(16)} \approx (1.06)$. By definition, the highest neutron rate occurs *at* the bang time. Therefore, the static profiles need to be depressed. This is handled by replacing the temporal integral with $\tau' = c\tau$, where the constant $c \approx 1.1$ has been determined by imposing $c \equiv Y/(\tau \dot{Y}_{\mathrm{bt}})$ and examining an ensemble of 1D simulations. This accounts for the aforementioned 6 % increase, along with an additional correction for deviations from Gaussian shape in the neutron signal.

We assume the pressure and temperature to be isotropic, and reconstruct the spatial dependence of these quantities Q by representing them as a dimensionless "shape function" $\hat{Q}(r)$, multiplied by a central value Q_0 possessing the dimension of Q,

$$Q(r,\theta,\phi) \approx Q_0 \hat{Q}(r)$$

$$\hat{Q}(r=0) = 1.$$

If we also normalize the radial coordinate with the hot-spot radius $x \equiv r/R_{\mathrm{hs}}$, then the recovered function $\hat{Q}(x)$ can be taken directly from *LILAC* simulations. That is, we assume that while the magnitude of the pressure, temperature etc. differ between experiment and simulation, their *shapes* should be similar.

Using this new formulation, the yield can be rewritten as

$$Y_{\mathrm{n}} = b\tau' \left(\frac{{P_{0,\mathrm{i}}}^2}{{T_{0,\mathrm{i}}}^2} \right) \int_0^{R_{\mathrm{hs}}} r^2 \frac{\hat{P}_{\mathrm{i}}^2}{\hat{T}_{\mathrm{i}}^2} \langle \sigma v \rangle \, \mathrm{d}r, \tag{10}$$

where $b = \left(4\pi f_{\mathrm{D}} f_{\mathrm{T}} / {k_{\mathrm{B}}}^2\right)$. Typically the ice layer of an OMEGA target has a D:T ratio of 40:60, while the vapor is 50:50. In order to settle on a single number for each species fraction, *LILAC* simulations are used to estimate the percentage of yield coming from the vapor and ice, respectively. The appropriate weighting factors are then used to converge on the hot-spot composition. The radial integral in equation (10) is taken from the target origin to the hot-spot boundary. Because the transition from hot spot to cold shell is continuous, the value input as the hot-spot edge must be chosen with care. Ideally, this would be acquired via neutron imaging. Although the Omega Laser Facility does not currently have neutron imaging, x rays can be used instead to find the desired volume. Historically, this is given by the x-ray R_{17} value, i.e., the radius at which the x-ray self-emission intensity has decreased to 17 % of the maximum intensity. Previous work by Cao *et al.*[53] shows that photons with energies between 15 and 20 keV are emitted from the same region that produces DT neutrons. Each channel of the spatially resolved electron temperature (SRTe) diagnostic is sensitive to a different photon energy range. The strongest correlation between the R_{17} and the neutron-producing region for shots with temperatures $\sim$ 5 keV is observed from synthetic data of the SRTe's fourth channel, which detects x rays with $E_\gamma \sim 20$ keV. These synthetic data show that in simulations, the region enclosed by the R_{17} from SRTe channel 4 accounts for the vast majority of the neutron source, ranging between 93% and 95% in high-velocity implosions. The x-ray R_{17} is valid even in the presence of ellipticity in the hot-spot shape, as it is obtained from a two-dimensional super-Gaussian fit. However, it should be noted that the majority of recent high-performing implosions are round and exhibit negligible ellipticity. An experimental SRTe image of shot 102154 is given in figure 6, which has a semi-major axis to semi-minor axis ratio $a/b = 1.03 \pm 0.02$.

From the neutron time-of-flight (nTOF) spectrum, a burn-averaged ion temperature can be extracted, which has the form

$$\langle T_{\mathrm{i}} \rangle = \frac{\int \mathrm{d}t \int \mathrm{d}^3 r \, T_{\mathrm{i}} n_{\mathrm{D}} n_{\mathrm{T}} \langle \sigma v \rangle}{\int \mathrm{d}t \int \mathrm{d}^3 r \, n_{\mathrm{D}} n_{\mathrm{T}} \langle \sigma v \rangle}. \tag{11}$$

Applying each of the previous approximations leads to a central ion temperature given by

$$T_{0,\mathrm{i}} = \langle T_{\mathrm{i}} \rangle \frac{\int_0^1 x^2 \left(\hat{P}_{\mathrm{i}}/\hat{T}_{\mathrm{i}}\right)^2 \langle \sigma v \rangle \, \mathrm{d}x}{\int_0^1 x^2 \left(\hat{P}_{\mathrm{i}}^2/\hat{T}_{\mathrm{i}}\right) \langle \sigma v \rangle \, \mathrm{d}x}. \tag{12}$$

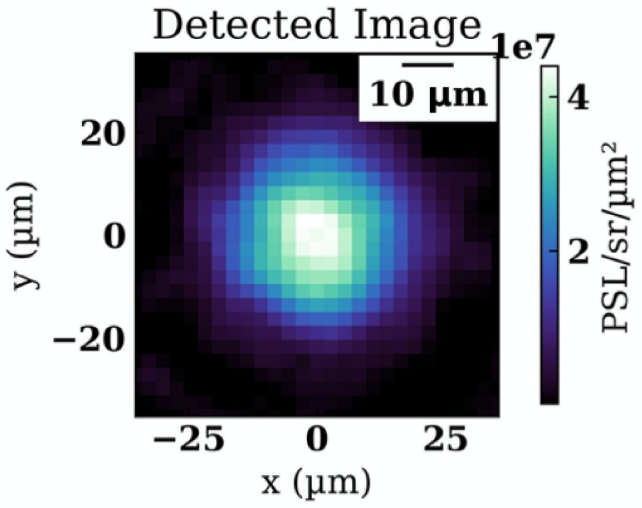

FIG. 6:
Spatially resolved electron temperature diagnostic (SRTe) image of shot 102154. Fourier analysis of the hot-spot modes show that the $\ell = 2$ mode is typically dominant in OMEGA implosions, and the inferred hot-spot volumes account for ellipticity. The majority of recent high-yield OMEGA implosions are round, with low semi-major to semi-minor axis ratios a/b. For example, shot 102154 has $a/b = 1.03 \pm 0.02$.

Now that an expression for the central ion temperature has been found, the yield equation can be inverted to isolate the central pressure

$$P_{0,\mathrm{i}} = b^{-1/2}\langle T_\mathrm{i}\rangle R_{17}^{-3/2}\sqrt{\frac{Y_\mathrm{n}}{\tau'}}\frac{\sqrt{\int_0^1 x^2\left(\hat{P}_\mathrm{i}/\hat{T}_\mathrm{i}\right)^2\langle\sigma v\rangle\,\mathrm{d}x}}{\int_0^1 x^2\left(\hat{P}_\mathrm{i}^2/\hat{T}_\mathrm{i}\right)\langle\sigma v\rangle\,\mathrm{d}x}. \quad (13)$$

The contribution to the hot-spot internal energy coming specifically from the ions is then simply given by integrating the ion pressure over the volume of the hot-spot. The result is

$$E_\mathrm{hs}^\mathrm{ion} = \frac{3}{2}(4\pi R_{17}^3)P_{0,\mathrm{i}}\int_0^1 x^2\hat{P}_\mathrm{i}\,\mathrm{d}x. \quad (14)$$

The rebound shock and subsequent compression of the hot spot preferentially heat the ions over the electrons. Since the equilibration time between ions and electrons is longer than the burnwidth, the electron temperature is below the ion temperature throughout the hot-spot (in the cold shell the temperatures are similar due to the faster equilibration time). In a characteristic hot-spot plasma, the Debye length is much shorter than the temperature and density gradient scale lengths; we therefore have the freedom to impose quasi-neutrality $n_\mathrm{i}(r) = n_\mathrm{e}(r)$. This means that the ratio of species pressures at any location is equal to the ratio of temperatures at that same point, including the center value. If we can calculate $T_\mathrm{rat} \equiv T_\mathrm{e}(0)/T_\mathrm{i}(0) = P_\mathrm{e}(0)/P_\mathrm{i}(0)$, we will be able to immediately determine the electronic contribution to the hot-spot internal energy.

From the ideal gas EOS,

$$T_\mathrm{e}(r) = P_\mathrm{e}(r)\frac{T_\mathrm{i}(r)}{P_\mathrm{i}(r)} = P_{0,\mathrm{i}}\frac{T_{0,\mathrm{e}}}{T_{0,\mathrm{i}}}\hat{P}_\mathrm{e}T_{0,\mathrm{i}}\frac{\hat{T}_\mathrm{i}}{P_{0,\mathrm{i}}\hat{P}_\mathrm{i}},$$

or, in terms of our desired variable T_rat,

$$T_\mathrm{e}(r) = T_{0,\mathrm{i}}T_\mathrm{rat}\hat{T}_\mathrm{i}\frac{\hat{P}_\mathrm{e}}{\hat{P}_\mathrm{i}}. \quad (15)$$

It is most useful to connect the central temperature ratio to another experimental observable so as to add one more constraint to our system. In the same fashion as equation (11) defines the neutron-averaged ion temperature, a neutron-averaged electron temperature appears as

$$\langle T_\mathrm{e}\rangle = \frac{\int \mathrm{d}t\int \mathrm{d}^3r\,T_\mathrm{e}n_\mathrm{D}n_\mathrm{T}\langle\sigma v\rangle}{\int \mathrm{d}t\int \mathrm{d}^3r\,n_\mathrm{D}n_\mathrm{T}\langle\sigma v\rangle}. \quad (16)$$

Eliminating the electron temperature with equation (15) and applying the same general assumptions and change of variables as before leads to

$$\langle T_\mathrm{e}\rangle = T_{0,\mathrm{i}}T_\mathrm{rat}\frac{\int_0^1 x^2\hat{P}_\mathrm{e}\left(\hat{P}_\mathrm{i}/\hat{T}_\mathrm{i}\right)\langle\sigma v\rangle\,\mathrm{d}x}{\int_0^1 x^2\left(\hat{P}_\mathrm{i}/\hat{T}_\mathrm{i}\right)^2\langle\sigma v\rangle\,\mathrm{d}x}. \quad (17)$$

It is now beneficial to use equation (17) and equation (12) to rewrite the temperature ratio in terms of the measured quantities and integrals of known radial profiles. Utilizing equation (13), we obtain the total hot-spot internal energy, represented here in its full, explicit form

$$E^\mathrm{hs} = k_\mathrm{B}\langle T_\mathrm{i}\rangle R_{17}^{3/2}\sqrt{\frac{9\pi Y_\mathrm{n}}{f_\mathrm{D}f_\mathrm{T}\tau'}}\frac{\sqrt{\int_0^1 x^2\left(\hat{P}_\mathrm{i}/\hat{T}_\mathrm{i}\right)^2\langle\sigma v\rangle\,\mathrm{d}x}}{\int_0^1 x^2\left(\hat{P}_\mathrm{i}^2/\hat{T}_\mathrm{i}\right)\langle\sigma v\rangle\,\mathrm{d}x}\left[\int_0^1 x^2\hat{P}_\mathrm{i}\,\mathrm{d}x + \frac{\langle T_\mathrm{e}\rangle}{\langle T_\mathrm{i}\rangle}\frac{\int_0^1 x^2\left(\hat{P}_\mathrm{i}^2/\hat{T}_\mathrm{i}\right)\langle\sigma v\rangle\,\mathrm{d}x}{\int_0^1 x^2\hat{P}_\mathrm{e}\left(\hat{P}_\mathrm{i}/\hat{T}_\mathrm{i}\right)\langle\sigma v\rangle\,\mathrm{d}x}\int_0^1 x^2\hat{P}_\mathrm{e}\,\mathrm{d}x\right]. \quad (18)$$

While the model presented here has been constructed primarily to calculate the hot-spot energy, the information that must be gathered in order to make that determination can be used to infer other quantities as well. These include scalar quantities like hot-spot mass, as well as radial profiles like specific reaction rate (equation (7)), or reaction rate linear

density $4\pi n_D n_T \langle \sigma v \rangle r^2$. Uncertainties in the model-estimated parameters are obtained by Monte Carlo sampling, assuming the uncertainties on the experimental inputs are normally distributed.

Experimental Diagnostics

Several important measurements need to be made in order to properly infer the hot-spot internal energy. From equation (18), we see that measurements of average ion and electron temperature, hot-spot radius, burnwidth, and neutron yield constitute the requisite parameters for this calculation. This is made possible by the Omega Laser Facility's comprehensive suite of diagnostics. The energy spectrum obtained by neutron time-of-flight detectors[33] are able to reveal not only the DT and DD neutron yields, but the ion temperature as well. Cu-activation detectors[27] are also used to measure the neutron yield. Areal densities are measured on the nTOF via backscattered neutrons off of plasma ions, and on a magnetic recoil spectrometer[54] using forward scattering. Images of the hot spot are taken by the single line-of-sight time-resolved x-ray imager[32], Kirkpatrick–Baez framing camera, gated monochromatic x-ray imaging diagnostic, and spatially-resolved electron temperature diagnostic[34]. The burnwidth (duration) and bang time (time of peak neutron rate) are measured by the neutron temporal diagnostic[31].

ACKNOWLEDGMENTS

The authors thank Dr. Prav Patel for discussions regarding the relationship between neutron and x-ray emission.

This report was prepared as an account of work sponsored by an agency of the U.S. Government. Neither the U.S. Government nor any agency thereof, nor any of their employees, makes any warranty, express or implied, or assumes any legal liability or responsibility for the accuracy, completeness, or usefulness of any information, apparatus, product, or process disclosed, or represents that its use would not infringe privately owned rights. Reference herein to any specific commercial product, process, or service by trade name, trademark, manufacturer, or otherwise does not necessarily constitute or imply its endorsement, recommendation, or favoring by the U.S. Government or any agency thereof. The views and opinions of authors expressed herein do not necessarily state or reflect those of the U.S. Government or any agency thereof.

This work was performed at the Laboratory for Laser Energetics for the U.S. Department of Energy National Nuclear Security Administration under grant No. DE-NA 0003856.

Funding for the targets utilized in this study were provided by General Atomics and funded through the NNSA contract 89233119CNA000063.

DATA AVAILABILITY

Raw data presented in this work were generated at the Omega Laser Facility. Derived data supporting the findings of this study are available from the corresponding author upon reasonable request, and with permission from the Laboratory for Laser Energetics.

CONFLICT OF INTEREST

The authors have no conflicts to disclose.

[1] O. Hurricane, D. Callahan, D. Casey, P. Celliers, C. Cerjan, E. Dewald, T. Dittrich, T. Döppner, D. Hinkel, L. B. Hopkins, *et al.*, Nature **506**, 343 (2014).
[2] J. Nuckolls, L. Wood, A. Thiessen, and G. Zimmerman, Nature **239**, 139 (1972).
[3] R. Betti and O. Hurricane, Nature Phys **12**, 435–448 (2016).
[4] S. Atzeni and J. Meyer-Ter-Vehn, *The physics of inertial fusion: beam plasma interaction, hydrodynamics, hot dense matter*, Internat. Mono. Phys. (Clarendon Press, Oxford, 2004).
[5] R. S. Craxton, K. S. Anderson, T. R. Boehly, V. N. Goncharov, D. R. Harding, J. P. Knauer, R. L. McCrory, P. W. McKenty, D. D. Meyerhofer, J. F. Myatt, A. J. Schmitt, J. D. Sethian, R. W. Short, S. Skupsky, W. Theobald, W. L. Kruer, K. Tanaka, R. Betti, T. J. B. Collins, J. A. Delettrez, S. X. Hu, J. A. Marozas, A. V. Maximov, D. T. Michel, P. B. Radha, S. P. Regan, T. C. Sangster, W. Seka, A. A. Solodov, J. M. Soures, C. Stoeckl, and J. D. Zuegel, Physics of Plasmas **22**, 110501 (2015), https://doi.org/10.1063/1.4934714.
[6] J. Lindl, Physics of plasmas **2**, 3933 (1995).
[7] J. W. S. B. Rayleigh, *Scientific Papers: 1881-1887*, Vol. 2 (University Press, 1900).
[8] M. Brouillette, Annual Review of Fluid Mechanics **34**, 445 (2002).
[9] V. Gopalaswamy, R. Betti, and J. Knauer, Nature **565**, 581 (2019), https://doi.org/10.1038/s41586-019-0877-0.
[10] A. Lees, R. Betti, J. Knauer, V. Gopalaswamy, D. Patel, K. Woo, K. Anderson, E. Campbell, D. Cao, J. Carroll-Nellenback, *et al.*, Physical Review Letters **127**, 105001 (2021).
[11] A. Lees, R. Betti, J. P. Knauer, V. Gopalaswamy, D. Patel, K. M. Woo, K. S. Anderson, E. M. Campbell, D. Cao, J. Carroll-Nellenback, R. Epstein, C. J. Forrest, V. N. Goncharov, D. R. Harding, S. X. Hu, I. V. Igumenshchev, R. T. Janezic, O. M. Mannion, P. B. Radha, S. P. Regan, A. Shvydky, R. C. Shah, W. T. Shmayda, C. Stoeckl, W. Theobald, and C. A. Thomas, Physics of Plasmas **30**, 012709 (2023), https://pubs.aip.org/aip/pop/article-pdf/doi/10.1063/5.0106515/16663321/012709_1_online.pdf.
[12] J. Delettrez, R. Epstein, M. C. Richardson, P. A. Jaanimagi, and B. L. Henke, Phys. Rev. A **36**, 3926 (1987).
[13] V. Gopalaswamy, R. Betti, J. P. Knauer, A. Lees, D. Patel, A. R. Christopherson, I. V. Igumenshchev, D. Cao, K. S. Anderson, A. Shvydky, D. H. Edgell, O. M. Mannion, C. Thomas, W. Theobald, C. Stoeckl, S. P. Regan, V. N. Goncharov, R. Shah, and E. M. Campbell, Physics of Plasmas **28**, 122705 (2021), https://doi.org/10.1063/5.0056662.
[14] S. X. Hu, V. N. Goncharov, P. B. Radha, J. A. Marozas, S. Skupsky, T. R. Boehly, T. C. Sangster, D. D. Meyerhofer, and R. L. McCrory, Physics of Plasmas **17**, 102706 (2010), https://doi.org/10.1063/1.3491467.
[15] R. Ejaz, V. Gopalaswamy, and R. Betti, Bulletin of the American Physical Society **64** (2022).
[16] A. R. Christopherson, R. Betti, A. Bose, J. Howard, K. M. Woo, E. M. Campbell, J. Sanz, and B. K. Spears, Physics of Plasmas **25**, 012703 (2018), https://doi.org/10.1063/1.4991405.
[17] A. Christopherson, R. Betti, and J. Lindl, Physical Review E **99**, 021201 (2019).
[18] J. D. Lawson, Proceedings of the physical society. Section B **70**, 6 (1957).
[19] R. Betti, P. Chang, B. Spears, K. Anderson, J. Edwards, M. Fatenejad, J. Lindl, R. McCrory, R. Nora, and D. Shvarts, Physics of Plasmas **17**, 058102 (2010).
[20] C. Zhou and R. Betti, Physics of Plasmas **15**, 102707 (2008).

[21] A. Bose, K. Woo, R. Nora, and R. Betti, Physics of Plasmas **22**, 072702 (2015).

[22] V. N. Goncharov, T. C. Sangster, R. Betti, T. R. Boehly, M. J. Bonino, T. J. B. Collins, R. S. Craxton, J. A. Delettrez, D. H. Edgell, R. Epstein, R. K. Follett, C. J. Forrest, D. H. Froula, V. Yu. Glebov, D. R. Harding, R. J. Henchen, S. X. Hu, I. V. Igumenshchev, R. Janezic, J. H. Kelly, T. J. Kessler, T. Z. Kosc, S. J. Loucks, J. A. Marozas, F. J. Marshall, A. V. Maximov, R. L. McCrory, P. W. McKenty, D. D. Meyerhofer, D. T. Michel, J. F. Myatt, R. Nora, P. B. Radha, S. P. Regan, W. Seka, W. T. Shmayda, R. W. Short, A. Shvydky, S. Skupsky, C. Stoeckl, B. Yaakobi, J. A. Frenje, M. Gatu-Johnson, R. D. Petrasso, and D. T. Casey, Physics of Plasmas **21**, 056315 (2014), https://doi.org/10.1063/1.4876618.

[23] A. Zylstra, O. Hurricane, D. Callahan, A. Kritcher, J. Ralph, H. Robey, J. Ross, C. Young, K. Baker, D. Casey, *et al.*, Nature **601**, 542 (2022).

[24] A. L. Kritcher, A. B. Zylstra, D. A. Callahan, O. A. Hurricane, C. R. Weber, D. S. Clark, C. V. Young, J. E. Ralph, D. T. Casey, A. Pak, O. L. Landen, B. Bachmann, K. L. Baker, L. Berzak Hopkins, S. D. Bhandarkar, J. Biener, R. M. Bionta, N. W. Birge, T. Braun, T. M. Briggs, P. M. Celliers, H. Chen, C. Choate, L. Divol, T. Döppner, D. Fittinghoff, M. J. Edwards, M. Gatu Johnson, N. Gharibyan, S. Haan, K. D. Hahn, E. Hartouni, D. E. Hinkel, D. D. Ho, M. Hohenberger, J. P. Holder, H. Huang, N. Izumi, J. Jeet, O. Jones, S. M. Kerr, S. F. Khan, H. Geppert Kleinrath, V. Geppert Kleinrath, C. Kong, K. M. Lamb, S. Le Pape, N. C. Lemos, J. D. Lindl, B. J. MacGowan, A. J. Mackinnon, A. G. MacPhee, E. V. Marley, K. Meaney, M. Millot, A. S. Moore, K. Newman, J.-M. G. Di Nicola, A. Nikroo, R. Nora, P. K. Patel, N. G. Rice, M. S. Rubery, J. Sater, D. J. Schlossberg, S. M. Sepke, K. Sequoia, S. J. Shin, M. Stadermann, S. Stoupin, D. J. Strozzi, C. A. Thomas, R. Tommasini, C. Trosseille, E. R. Tubman, P. L. Volegov, C. Wild, D. T. Woods, and S. T. Yang, Phys. Rev. E **106**, 025201 (2022).

[25] A. B. Zylstra, A. L. Kritcher, O. A. Hurricane, D. A. Callahan, J. E. Ralph, D. T. Casey, A. Pak, O. L. Landen, B. Bachmann, K. L. Baker, L. Berzak Hopkins, S. D. Bhandarkar, J. Biener, R. M. Bionta, N. W. Birge, T. Braun, T. M. Briggs, P. M. Celliers, H. Chen, C. Choate, D. S. Clark, L. Divol, T. Döppner, D. Fittinghoff, M. J. Edwards, M. Gatu Johnson, N. Gharibyan, S. Haan, K. D. Hahn, E. Hartouni, D. E. Hinkel, D. D. Ho, M. Hohenberger, J. P. Holder, H. Huang, N. Izumi, J. Jeet, O. Jones, S. M. Kerr, S. F. Khan, H. Geppert Kleinrath, V. Geppert Kleinrath, C. Kong, K. M. Lamb, S. Le Pape, N. C. Lemos, J. D. Lindl, B. J. MacGowan, A. J. Mackinnon, A. G. MacPhee, E. V. Marley, K. Meaney, M. Millot, A. S. Moore, K. Newman, J.-M. G. Di Nicola, A. Nikroo, R. Nora, P. K. Patel, N. G. Rice, M. S. Rubery, J. Sater, D. J. Schlossberg, S. M. Sepke, K. Sequoia, S. J. Shin, M. Stadermann, S. Stoupin, D. J. Strozzi, C. A. Thomas, R. Tommasini, C. Trosseille, E. R. Tubman, P. L. Volegov, C. R. Weber, C. Wild, D. T. Woods, S. T. Yang, and C. V. Young, Phys. Rev. E **106**, 025202 (2022).

[26].

[27] J. A. Frenje, Plasma Physics and Controlled Fusion **62**, 023001 (2020).

[28] C. Cerjan, P. T. Springer, and S. M. Sepke, Physics of Plasmas **20**, 056319 (2013).

[29] A. B. Zylstra, R. Nora, P. Patel, and O. Hurricane, Physics of Plasmas **28**, 122703 (2021), https://doi.org/10.1063/5.0069366.

[30] C. A. Williams, R. Betti, V. Gopalaswamy, and A. Lees, Physics of Plasmas **28**, 122708 (2021), https://doi.org/10.1063/5.0069372.

[31] C. Stoeckl, R. Boni, F. Ehrne, C. J. Forrest, V. Y. Glebov, J. Katz, D. J. Lonobile, J. Magoon, S. P. Regan, M. J. Shoup, A. Sorce, C. Sorce, T. C. Sangster, and D. Weiner, Review of Scientific Instruments **87**, 053501 (2016), https://doi.org/10.1063/1.4948293.

[32] W. Theobald, C. Sorce, M. Bedzyk, S. T. Ivancic, F. J. Marshall, C. Stoeckl, R. C. Shah, M. Lawrie, S. P. Regan, T. C. Sangster, E. M. Campbell, T. J. Hilsabeck, K. Englehorn, J. D. Kilkenny, D. Morris, T. M. Chung, J. D. Hares, A. K. L. Dymoke-Bradshaw, P. Bell, J. Celeste, A. C. Carpenter, M. Dayton, D. K. Bradley, M. C. Jackson, L. Pickworth, S. R. Nagel, G. Rochau, J. Porter, M. Sanchez, L. Claus, G. Robertson, and Q. Looker, Review of Scientific Instruments **89**, 10G117 (2018), https://pubs.aip.org/aip/rsi/article-pdf/doi/10.1063/1.5036767/16728009/10g117_1_online.pdf.

[33] A. S. Moore, D. J. Schlossberg, B. D. Appelbe, G. A. Chandler, A. J. Crilly, M. J. Eckart, C. J. Forrest, V. Y. Glebov, G. P. Grim, E. P. Hartouni, R. Hatarik, S. M. Kerr, J. Kilkenny, and J. P. Knauer, Review of Scientific Instruments **94**, 061102 (2023), https://pubs.aip.org/aip/rsi/article-pdf/doi/10.1063/5.0133655/17977864/061102_1_5.0133655.pdf.

[34] K. Churnetski, K. M. Woo, W. Theobald, P. B. Radha, R. Betti, V. Gopalaswamy, I. V. Igumenshchev, S. T. Ivancic, M. Michalko, R. C. Shah, C. Stoeckl, C. A. Thomas, and S. P. Regan, Review of Scientific Instruments **93**, 093530 (2022), https://pubs.aip.org/aip/rsi/article-pdf/doi/10.1063/5.0098977/16603737/093530_1_online.pdf.

[35] O. M. Mannion, I. V. Igumenshchev, K. S. Anderson, R. Betti, E. M. Campbell, D. Cao, C. J. Forrest, M. G. Johnson, V. Y. Glebov, V. N. Goncharov, V. Gopalaswamy, S. T. Ivancic, D. W. Jacobs-Perkins, A. Kalb, J. P. Knauer, J. Kwiatkowski, A. Lees, F. J. Marshall, M. Michalko, Z. L. Mohamed, D. Patel, H. G. Rinderknecht, R. C. Shah, C. Stoeckl, W. Theobald, K. M. Woo, and S. P. Regan, Physics of Plasmas **28**, 042701 (2021), https://doi.org/10.1063/5.0041554.

[36] S. Skupsky, R. W. Short, T. Kessler, R. S. Craxton, S. Letzring, and J. M. Soures, Journal of Applied Physics **66**, 3456 (1989), https://doi.org/10.1063/1.344101.

[37] I. V. Igumenshchev, D. H. Edgell, V. N. Goncharov, J. A. Delettrez, A. V. Maximov, J. F. Myatt, W. Seka, A. Shvydky, S. Skupsky, and C. Stoeckl, Physics of Plasmas **17**, 122708 (2010), https://doi.org/10.1063/1.3532817.

[38] J. Baltazar, R. Betti, K. Churnetski, V. Gopalaswamy, J. P. Knauer, D. Patel, H. G. Rinderknecht, R. C. Shah, C. Stoeckl, C. A. Williams, and S. P. Regan, Review of Scientific Instruments **93**, 123513 (2022), https://doi.org/10.1063/5.0101653.

[39] W. Kruer, *The physics of laser plasma interactions* (crc Press, 2019).

[40] W. Seka, D. H. Edgell, J. F. Myatt, A. V. Maximov, R. W. Short, V. N. Goncharov, and H. A. Baldis, Physics of Plasmas **16**, 052701 (2009), https://doi.org/10.1063/1.3125242.

[41] A. Christopherson, R. Betti, C. Forrest, J. Howard, W. Theobald, J. Delettrez, M. Rosenberg, A. Solodov, C. Stoeckl, D. Patel, *et al.*, Physical Review Letters **127**, 055001 (2021).

[42] A. Christopherson, R. Betti, C. Forrest, J. Howard, W. Theobald, E. Campbell, J. Delettrez, M. Rosenberg, A. Solodov, C. Stoeckl, *et al.*, Physics of Plasmas **29**, 122703 (2022).

[43] A. Zylstra, A. Kritcher, O. Hurricane, D. Callahan, K. Baker, T. Braun, D. Casey, D. Clark, K. Clark, T. Döppner, *et al.*, Physical Review Letters **126**, 025001 (2021).

[44] O. A. Hurricane, D. A. Callahan, P. T. Springer, M. J. Edwards, P. Patel, K. Baker, D. T. Casey, L. Divol, T. Döppner, D. E. Hinkel, L. F. B. Hopkins, A. Kritcher, S. L. Pape, S. Maclaren, L. Masse, A. Pak, L. Pickworth, J. Ralph, C. Thomas, A. Yi, and A. Zylstra, Plasma Physics and Controlled Fusion **61**, 014033 (2018).

[45] R. Betti, K. Anderson, V. N. Goncharov, R. L. McCrory, D. D. Meyerhofer, S. Skupsky, and R. P. J. Town, Physics of Plasmas **9**, 2277 (2002), https://doi.org/10.1063/1.1459458.

[46] K. M. Woo, R. Betti, D. Shvarts, A. Bose, D. Patel, R. Yan, P.-Y. Chang, O. M. Mannion, R. Epstein, J. A. Delettrez, M. Charissis, K. S. Anderson, P. B. Radha, A. Shvydky, I. V. Igumenshchev, V. Gopalaswamy, A. R. Christopherson, J. Sanz, and H. Aluie, Physics of Plasmas **25**, 052704 (2018), https://doi.org/10.1063/1.5026706.

[47] K. Anderson and R. Betti, Physics of Plasmas **10**, 4448 (2003), https://doi.org/10.1063/1.1616559.

[48] V. N. Goncharov, J. P. Knauer, P. W. McKenty, P. B. Radha, T. C. Sangster, S. Skupsky, R. Betti, R. L. McCrory, and D. D. Meyerhofer, Physics of Plasmas **10**, 1906 (2003), https://doi.org/10.1063/1.1562166.

[49] K. Anderson and R. Betti, Physics of Plasmas **11**, 5 (2004), https://doi.org/10.1063/1.1632903.

[50] J. P. Knauer, K. Anderson, R. Betti, T. J. B. Collins, V. N. Goncharov, P. W. McKenty, D. D. Meyerhofer, P. B. Radha, S. P. Regan, T. C. Sangster, V. A. Smalyuk, J. A. Frenje, C. K. Li, R. D. Petrasso, and F. H. Séguin, Physics of Plasmas **12**, 056306 (2005), https://doi.org/10.1063/1.1882332.

[51] R. Betti, K. Anderson, J. Knauer, T. Collins, R. McCrory, P. McKenty, and S. Skupsky, Physics of plasmas **12**, 042703 (2005).

[52] S. P. Regan, V. N. Goncharov, I. V. Igumenshchev, T. C. Sangster, R. Betti, A. Bose, T. R. Boehly, M. J. Bonino, E. M. Campbell, D. Cao, T. J. B. Collins, R. S. Craxton, A. K. Davis, J. A. Delettrez, D. H. Edgell, R. Epstein, C. J. Forrest, J. A. Frenje, D. H. Froula, M. Gatu Johnson, V. Y. Glebov, D. R. Harding, M. Hohenberger, S. X. Hu, D. Jacobs-Perkins, R. Janezic, M. Karasik, R. L. Keck, J. H. Kelly, T. J. Kessler, J. P. Knauer, T. Z. Kosc, S. J. Loucks, J. A. Marozas, F. J. Marshall, R. L. McCrory, and

P. W. McKenty, Phys. Rev. Lett. **117**, 059903 (2016).
[53]D. Cao, R. C. Shah, S. P. Regan, R. Epstein, I. V. Igumenshchev, V. Gopalaswamy, A. R. Christopherson, W. Theobald, P. B. Radha, and V. N. Goncharov, Physics of Plasmas **26**, 082709 (2019), https://pubs.aip.org/aip/pop/article-pdf/doi/10.1063/1.5112759/15855135/082709_1_online.pdf.
[54]M. Gatu Johnson, Review of Scientific Instruments **94**, 021104 (2023), https://pubs.aip.org/aip/rsi/article-pdf/doi/10.1063/5.0127438/16681141/021104_1_online.pdf.
[55]A. R. Christopherson, O. A. Hurricane, C. Weber, A. Kritcher, R. Nora, J. Salmonson, R. Tran, J. Milovich, S. Maclaren, D. Hinkel, and R. Betti, Physics of Plasmas **30** (2023), 10.1063/5.0140888, 062705, https://pubs.aip.org/aip/pop/article-pdf/doi/10.1063/5.0140888/17979721/062705_1_5.0140888.pdf.